

STUDY OF TRANSIENT FLOW AND PARTICLE TRANSPORT IN CONTINUOUS STEEL CASTER MOLDS: PART II. PARTICLE TRANSPORT

Quan Yuan, Brian G. Thomas and S.P. Vanka

University of Illinois at Urbana-Champaign,
Department of Mechanical and Industrial Engineering,
1206 West Green Street,
Urbana, IL USA 61801

Ph: 217-244-2859, 217-333-6919; Fax: 217-244-6534

Email: quanyuan@uiuc.edu, bgthomas@uiuc.edu, spvanka@uiuc.edu

ABSTRACT

Particle motion and capture in continuous steel casters were simulated using a Lagrangian trajectory-tracking approach, based on time-dependent flow fields obtained from large eddy simulations (Part I). A computation was first conducted on a water model of a full-scale standard slab caster, where measurements were available. It simulated the transport of 15,000 plastic particles, and their removal by a screen positioned near the mold top surface. The computation shows the screen removal fractions to be $27\pm 5\%$ for 0-10s and $26\pm 2\%$ for 10-100s, which agrees with previous measurements. The flow exiting the nozzle was relatively uniform, and turbulent motion in the domain was very chaotic, so particle removal did not depend on the initial location of particles introduced in the nozzle port. A computation of motion and capture of 40,000 small inclusions ($10\mu\text{m}$ and $40\mu\text{m}$) was then performed in an actual thin-slab steel caster. The particles moved through the mold region with an asymmetrical distribution, which was caused by transients in fluid turbulence in the lower recirculation region, rather than by inlet variations at the nozzle port. Only about 8% of these small particles were removed to the top surface. This removal fraction was independent of both particle size and density, likely because all the simulated particles were too small to deviate significantly from the surrounding fluid flow. Finally, the computational results were further processed to predict the ultimate distribution of impurity particles in the solid thin slab after a short burst of inclusions entered the mold. They were reprocessed to reveal the distribution of total oxygen content for a steady inclusion supply from the nozzle. The results of this work confirm the important role of flow transients in the transport and capture of particles during continuous casting, and can serve as a benchmark for future simplified models.

I. INTRODUCTION

Particle transport is an important phenomenon during continuous casting of steel slabs, as it significantly affects steel quality. During the continuous casting process, non-metallic inclusions such as deoxidation products (e.g. alumina), reoxidation products (from air exposure) and exogenous inclusions (e.g. loose dirt) may enter the molten steel.^[1] Impurity inclusions may also be generated from unexpected chemical reactions.^[1] As shown in Fig. 1, inclusions and argon bubbles may be carried by the jet into the mold cavity. Additional inclusions may be generated by excessive fluid velocity across the top surface, which shears off fingers of liquid slag to emulsify into the steel.^[2] In the mold cavity, molten steel freezes against the water

cooled mold to solidify into a shell, which grows and is continuously pulled downward at the casting speed. Inside the tapering domain enclosed by the shell, molten steel recirculates in the liquid pool. If this flow pattern can carry the impurity inclusions to the top surface, they may be removed into the liquid slag layer. Otherwise, they will eventually be trapped by the solidification front and cause defects in the final product. If they are detected, defects caused by inclusions lower the yield. Otherwise, inclusions degrade steel quality by lowering the minimum strength, fatigue life, and surface appearance.

Flow in the liquid pool is highly turbulent involving complex time-dependent structures, as discussed in Part I of this paper.^[3] This turbulent flow plays an important role in transporting impurity inclusions. If the fluid generates excessive level fluctuations or insufficient liquid temperatures on the top surface, particles are likely to be captured by the solidifying meniscus before they can enter the liquid slag layer. Studies suggest that those particles trapped near the meniscus generate surface delamination, and may initiate surface cracks.^[4] Particles which are entrained into the lower recirculation zone by the fluid can gradually spiral and may be trapped by the solidification front, leading to intermittent defects such as internal cracks, slivers and blisters in the final rolled products.^[5] Experimental studies have confirmed that these intermittent quality problems are associated with the time-dependent flow in the liquid pool.^[5] One way to lower defects from internal inclusions is to avoid detrimental flow patterns in the liquid pool, such as by optimizing the nozzle design. This requires fundamental understanding of the particle flow during continuous casting. The present work aims at gaining insights into particle transport in the continuous casting liquid pool using advanced computational tools.

With the high operating temperature of continuous casting, computational modeling is the most feasible tool for understanding liquid-particle flow in this complex process. Mathematical modeling of liquid-particle flow can be classified into Eulerian and Lagrangian approaches, according to the manner in which the particle phase is treated.^[6] The former approach solves transport equations of continuum particle concentration in an Eulerian framework, while the latter tracks motion of each single particle. Both approaches have been extensively applied to simple model problems involving particle-laden flows.^[7-12] However, only a few computational studies have been performed on inclusion transport in the continuous casting process. Grimm et al.^[13] simulated inclusion motion and separation in the continuous casting liquid pool by solving an extra transport equation for continuum particle volume concentration, based on a constant Schmidt number of one.^[13, 14] The fluid velocity field was computed using the k - ϵ model. The particle convective velocity was modeled by adding the time-averaged local fluid velocity and the particle terminal velocity, which was the only parameter used to distinguish different particles. The effects of fluid turbulence on particle motion were not modeled. The crucial inclusion-capture criterion simply assumed that particles are trapped once they touch the solidification front. No quantitative validation was given.

Due to the low volume fraction of impurity inclusions in continuous casting, transport of inclusions can also be computed via a one-way coupled Lagrangian approach, as done in a few previous studies.^[15-19] In those studies, trajectories of several hundred particles were calculated to obtain statistics on particle removal and capture. The time-averaged fluid velocities, computed using the k - ϵ model, were employed to calculate the forces exerted by the fluid on the particles. To account for the effect of fluid turbulence, each particle velocity incorporates a velocity component due to random fluctuations, obtained using models such as the random-walk model.^[14, 16] These previous studies provide valuable insight. However, their modeling of the fluid velocity field and the effect of fluid turbulence on particle transport have not been

validated. In addition, it is unclear whether only a few hundred particles can produce reliable statistics.

Modeling of liquid-particle flow can be classified as “one-way” coupling, where the flow affects the particle motion, or “two-way” coupling, if the particles also modify the flow. Comprehensive reviews of this are given elsewhere.^[20, 21] Two-way coupling is important for gas flows with heavy particles, which tend to concentrate in regions of high $\nabla \mathbf{v} : \nabla \mathbf{v}$ and compressional strain and regions of low swirling strength.^[21] However, one-way coupling is appropriate even for heavy particles, if the particle volume fraction is less than 0.1%.^[22] Thus, one-way coupling is sufficient in processes such as continuous casting, where the particle density is close to the fluid density (3:7), and volume fractions are very small.

This work first computes Lagrangian motion of 15,000 plastic particles in a full-scale standard slab water model, using a time-dependent fluid velocity field obtained from Large Eddy Simulations (LES) in Part I (*Case 1*).^[3] The predictions are validated by comparing with measurements. The model is next applied to simulate transport and capture of small inclusions (10 μm and 40 μm) in an actual thin-slab steel caster (*Case 2-S* in Part I).^[3] A preliminary inclusion capture criterion is employed, which considers critical dendrite growth velocity, inclusion size, primary dendrite arm spacing (PDAS) and local cross-flow velocity. Particle flow behavior, removal and entrapment fractions are quantified. Finally, the locations of captured particles and distribution of total oxygen in the final steel slab are predicted based on the simulation results.

II. MODEL DESCRIPTION

Fluid flow and particle transport are computed in model domains (see Fig. 2) that include the liquid pool of a 2.15m water model (*Case 1*), and the submerged entry nozzle and the top 2.4m of a steel strand (*Case 2-S*). Three dimensional time-dependent turbulent fluid velocities are first obtained by solving the Navier-Stokes equations, as described in Part I.^[3] Special velocity boundary conditions^[3] are applied to the fluid at the solidifying front in the steel caster to simulate the solidification effects. The transport of inclusion particles through this flow field is then modeled as follows.

A. Governing Equations

Particle transport is solved by integrating the following equations in a Lagrangian framework:

$$\mathbf{v}_p = \frac{d\mathbf{x}_p}{dt} \quad [1]$$

$$\frac{d\mathbf{v}_p}{dt} = \frac{18\rho\nu_0}{\rho_p d_p^2} \left(1 + 0.15 \text{Re}_p^{0.687}\right) (\mathbf{v} - \mathbf{v}_p) + \left(1 - \frac{\rho}{\rho_p}\right) \mathbf{g} + \frac{\mathbf{F}_{saff}}{m_p} \quad [2]$$

where:

$$\mathbf{g} = (0, 0, 9.81\text{m/s}^2) \quad [3]$$

$$\text{Re}_p = \frac{|\mathbf{v} - \mathbf{v}_p| d_p}{\nu_0} \quad [4]$$

$$\mathbf{F}_{saff} = 1.61d_p^2 (\mu_0 \rho)^{1/2} |\boldsymbol{\omega}|^{-1/2} [(\mathbf{v} - \mathbf{v}_p) \times \boldsymbol{\omega}] \quad [5]$$

$$\text{and} \quad \boldsymbol{\omega} = \nabla \times \mathbf{v} \quad [6]$$

The three terms on the RHS of Eq. [2] are due to the forces of drag (for $Re_p < 800$), ^[23] buoyancy (due to density difference) and Saffman lift (due to shear velocity gradients) ^[23] for spherical particles. Re_p is the particle Reynolds number for creeping flow, based on the small difference between the fluid and particle velocities.

B. Initial and Boundary Conditions

Inclusions were introduced into the computational domain at the local fluid velocity. Their positions were chosen randomly in the plane of the nozzle outlet ports (*Case 1*) or in the edges of a cylindrical region in the tundish above the submerged entry nozzle (*Case 2-S*). The results of a separate simulation of fluid flow and particle trajectories in the nozzle itself were used to determine the particle locations in the nozzle outlet port planes for the caster simulation (*Case 2-S*). Elastic re-bounce was assumed when inclusions hit the plastic wall of the water model (*Case 1*). Inclusions touching the top surface were assumed to be removed.

C. Modeling of Particle Capture by the Solidification Front

In an actual steel caster (*Case 2-S*), inclusions may be trapped when they touch the side boundaries, which represent the solidification front. The capture of inclusions by an advancing solidification front involves complex phenomena which have been investigated in many previous studies. ^[24-30] Particles were reported to be pushed along by the moving front unless the solidification exceeds a critical velocity to engulf them. ^[24-26] ^[29, 30] Unfortunately, the capture criterion proposed in those fundamental studies can not be directly applied to continuous casting for two main reasons. Firstly, the solidifying melt was stationary in those studies, compared to the strong inertia-driven flow in the liquid pool of the continuous caster. Cross flow enhances particle pushing, ^[28] whose mechanism is not fully understood. Secondly, the solidification fronts in those studies had a smooth curvature, which contrasts with the dendritic front shape in continuous cast steel. Experimental studies have found that particle capture and pushing depend greatly on the morphology of the solidification front. ^[31] Specifically, inclusions small enough to enter the gap between two dendrite arms are eventually captured by a mechanism called “entrapment”. ^[31] Entrapment occurs at solidification speeds much lower than the critical velocity for engulfment. ^[31] Fundamental criteria for particle capture in continuous casting are being developed as part of a larger project. The effects of critical dendrite growth velocity, particle size, primary dendrite arm spacing (PDAS) and local cross-flow velocity all are being considered. ^[32] The present work focuses on particles smaller than the PDAS which can easily enter in between primary dendrite arms and become entrapped with little chance of being pushed away regardless of solidification front velocity. ^[32] Previous measurements (Fig. 3) ^[33] show that the PDAS is smallest near the top surface (about 50 μ m) and increases along the casting direction as the solidification rate slows. Thus, this work investigates 10 μ m and 40 μ m particles which are predicted to become entrapped instantly upon touching the solidification front.

D. Solution Procedure

The particle transport equations were integrated using the fourth order Runge-Kutta method. ^[34] Particle velocities and displacements were solved at every time step after the fluid velocity field was solved. The local fluid velocity in the drag and lift terms of Eq. [2] was interpolated from the nearest neighbor cells using a second order scheme. ^[34] Due to the low

volume fraction of impurity inclusions for the continuous casting process ($\sim 0.01\%$ for a typical steel with 30ppm oxygen), one-way coupling was employed, which neglects the modification of fluid turbulence by the particles. The removal, re-bound (*Case 1*) and capture criteria (*Case 2-S*) were tested whenever a particle crossed a domain boundary.

E. Computational Details

Two computations were performed in this work, which are described as follows.

1. Water Model Validation

The first computation (*Case 1*) calculated the transport of 17,500 spherical particles in a full-scale standard slab water model (Fig. 2(a)), to compare with particle removal fractions measured previously for conditions given in Table I.^[17] In the experiments, around 8,000-30,000 elliptical disk-shaped plastic beads were injected into the liquid pool with water through the nozzle over a few seconds. The density and size of the beads were chosen to aid visualization while approximating the vertical terminal velocity expected of typical $300\mu\text{m}$ alumina inclusions in liquid steel. To model the removal of inclusion particles to the top surface, a screen was positioned near the top surface and the SEN (see Fig. 4) to trap plastic beads as they flowed across the top surface towards the SEN and headed downwards. The experiments were repeated at least five times and the average inclusion removal fraction by the screen was reported elsewhere.^[17]

Only half of the water model was modeled to reduce computational cost. The capture of particles by the screen was modeled by summing the particles that crossed the screen from the top. The screen influenced neither the fluid velocity field (Part I)^[3] nor the particle transport. The particles were divided into five groups of 500 particles and another six groups of 2,500 particles, in order to investigate statistical variations and the effect of the number of particles. The particles were injected into the nozzle ports over the time periods given in Table II.

2. Inclusion Transport in a Thin-Slab Steel Caster

In the second computation (*Case 2-S*), the transport and capture of four groups of 10,000 small inclusions, with two different sizes ($10\mu\text{m}$ and $40\mu\text{m}$) and two different densities (2700 kg/m^3 and 5000 kg/m^3), were simulated in an actual thin slab steel caster (Fig. 2(b)). These inclusions could represent entrained mold slag or alumina particles, with varying amounts of entrained steel filling internal voids and thus raising its density. The computational domain has two portions. The nozzle domain includes part of the bottom of the tundish and the entire 1.11m long trifurcated submerged entry nozzle. The strand domain includes the top 2.4m of the molten pool in the mold and strand. This 2.4m computational domain is part of the 3m straight section of the caster. In contrast with the water model, the steel caster has no solid bottom wall. The shape of the internal liquid pool domain was curved to account for the shell, and had mass flowing through it to represent solidification. The shell thickness increases from 0 at the meniscus to 26mm (wide face) or 25mm (narrow face) at domain exit (Fig. 3 in Part I).^[3] The two different densities assigned to the particles represent different fractions of molten steel in the inclusion.^[35] The 40,000 computed particles were introduced into the three nozzle port outlet planes over 9s (33-42s of the fluid simulation). More information on casting conditions, material properties and computational parameters on both cases is given in Table I.

3. Time Step Selection and Computational Cost

The time step for integrating the particle trajectories was chosen based on the velocity response time of the particle. Response time indicates how fast a particle responds to a velocity change of the surrounding fluid and is calculated as follows:^[23]

$$\iota_v = \frac{\rho_p d_p^2}{18\mu_0} \quad [7]$$

Small particles with a small density have the smallest response time. The same time step used in the fluid velocity computation (0.0008s) was employed for *Case 1*, where the particle response time is very large (0.79s). However, in the actual steel caster simulation (*Case 2-S*), the time steps were smaller than that of the fluid simulation (0.001s), and varied for different particles. The smallest time step for the particle simulation was 2×10^{-6} seconds, for the $10\mu\text{m}$, 2700 kg/m^3 particles, which had the smallest response time of only $2.68 \times 10^{-6} \text{ s}$. This required 500 time steps of particle motion within each step of the fluid velocity computation.

Simulations of particle transport are less computationally demanding than flow simulations. The particle computation of *Case 1* took 2.4 additional CPUs per time step (0.0008s) for 17,500 particles on a Pentium III 750Hz PC, compared to the 19.2 CPUs per step for the flow simulation (1.4M cells). However, the small time steps in *Case 2-S* greatly slowed the overall computational performance. Both the flow simulations (1.3M cells) and the transport of 40,000 particles took 29.2 CPUs per fluid time step (0.001s).

III. STANDARD-SLAB WATER-MODEL RESULTS

The computational model was first applied to simulate particle transport in a standard thickness (250mm) slab water model (Fig. 2(a)), ^[17, 36] in which measurements on particle removal are available. ^[17] The time-dependent fluid velocity field in this water model was obtained from a large eddy simulation, details of which can be found in Part I (*Case 1*). ^[3]

A. Particle Distributions

The transport of six groups of 2,500 particles and five groups of 500 particles were simulated, as described in Section II. The four snapshots in Fig. 4 reveal the distribution of all six groups of 2,500 particles (15,000 particles) together at four time instants. A video of the transient particle motion is available elsewhere. ^[37] The extended line inside the liquid pool shows the position of the screen used to capture particles. This figure shows that particles move within the jet after injection (Fig. 4(a)) and split into two parts (Fig. 4(b)), corresponding to the upper and lower rolls, after they hit the narrow face. By 100s (Fig. 4(d)), the particles are well dispersed throughout the domain. Some of the particles flow along the top surface and are removed. Other particles flow out of the mold bottom with the outflow fluid and represent particles that would be trapped deeper in the steel caster, leading to defects in the solid steel strand.

B. Representative Particle Trajectories

Typical trajectories of four particles are shown in Fig. 5 for 100s of computation or until they contact the top surface (first frame) or exit the domain (second frame). Particles in the last two frames are still moving. While moving with the flow, the particles gradually drift upward, with a typical particle Reynolds number of 10, which validates the assumption in Eq. [2]. These irregular trajectories illustrate the effect of turbulent fluid motion on particle transport.

C. Particle Removal

It is sometimes postulated that particles exiting the top portion of the nozzle should have a better chance to be removed to the top surface. This is examined in Fig. 6. Figure 6(a) shows the initial positions of all 15,000 particles at the nozzle port exit plane. Figures 6(b) and (c)

reveal the initial positions of particles which were removed to the top surface during 0s-10s and 10s-100s respectively. Time starts at injection of the first particle (0s). All three distributions are uniformly random, indicating that particle removal to the top surface is independent of its initial position. This is because turbulence within the jet and liquid pool makes the initial position irrelevant.

The simulated trajectories of the 15,000 particles were then processed to determine the fractions of particles removed to the top surface (lines) in Fig. 7, which are compared with measured fractions removed by the screen (symbols) in the water model. After 10s, approximately 23% of the particles are removed, and by 100s about 55% have been removed. Considering the uncertainties in the experiments, and variability in the turbulent computations, the agreement between the computational and experimental results within 5% is encouraging. The results also show that the screen appears to simulate surface removal well at early times, but under-predicts it at later times (100s). The computation suggests that the total removal fraction is very large (nearly 80%) when the walls are unable to trap particles.

D. Number of Particles for Reliable Statistics

The particle fractions removed by the screen for the 2,500 and 500 particle groups are presented in Table III, and are also compared with measurements. The average removal fractions for both groups agree with experiments within $\pm 5\%$. However, the removal fraction varies greatly between groups, especially for the first 10s after particles enter the mold. This is

reflected by the standard deviation, $(\sigma_u = \sqrt{\frac{\sum_{i=1}^N (u_i - u_{mean})^2}{N}})$ which decreases from 5.5% (500 particle groups) and 4.8% (2,500 particle groups) for 0-10s to 2.9% and 1.4% for 10-100s. The standard deviation of the 2,500 particle groups is always lower than that of the 500 particle groups, as expected due to the improvement in statistical confidence with increasing population size. However, the improvement is small for 0-10s. This suggests that during early times, particle removal is chaotic, because it is dominated by the turbulent eddies of the initial jet. To obtain a more reliable statistical estimate of the mean would require injecting particles during different time intervals. Increasing the number of particles improves the statistics at later times, (e.g. 10-100s) because the standard deviation drops in half. This is because the particles become well dispersed in the liquid pool and random statistics become valid.

IV. THIN-SLAB STEEL-CASTER RESULTS

After examining the accuracy of this computational model of particle transport in a standard-slab water model, it then was applied to investigate the transport and capture of small inclusions in an actual thin slab steel caster, in which a trifurcated nozzle is used. [3, 33, 38, 39] The fluid velocities were again obtained from a large eddy simulation (*Case 2-S* in Part I) [3] and conditions are given in Table I.

A. Particle Distributions

The simulation of the submerged entry nozzle revealed locations where particles touched an inner wall of the nozzle, shown in Fig. 8. About 16% of the particles exiting the tundish touched an inner wall of the nozzle and another 10% touched the stopper rod. These inclusions might stick to cause nozzle clogging in a real caster, depending on the properties of the nozzle material and thermodynamic reactions at the interface. Note that most of the inclusions touch the bottom portion of the stopper rod or the nozzle walls just below the stopper rod. This

coincides with the location of clogging sometimes observed in practice.^[40] Some particles touch the bottom of the SEN near the outlet ports. The distributions of the particles in the jets that exit the nozzle ports are shown in Fig. 9. This figure reveals that almost no particles exit from the top or bottom portions of the nozzle ports, which are regions of backflow where fluid enters the nozzle (see Part I).^[3]

Three snapshots of the particle distributions computed in the liquid pool are shown in Fig. 10, together with the locations of the particles that were entrapped by the solidification front. A video is available at <http://ccc.me.uiuc.edu>. Particles are seen to move with the jet and reach the narrow face about 0.6 seconds (33.6s total flow simulation time) after first injection (33.0s). The 40,000 particles split into two groups about 2 seconds after injection (33.0s) and enter the upper and lower rolls. After 15s, the particles in the upper rolls are well dispersed and the fastest have penetrated deep into the lower recirculation zone. Although the particles were symmetrically introduced from the nozzle port and had a relatively symmetrical distribution for approximately 10 seconds, a noticeable asymmetry is seen in this frame. This is caused directly by the flow asymmetry observed and reported in Part I (Fig. 27) of this paper.^[3] Specifically, the fluid had a larger downward velocity near the right-hand narrow face from 36-40s, which the particles follow. It was also shown in Part I that this time-varying asymmetry is not directly caused by the inflow asymmetries from nozzle, but originates from dynamic flow instabilities. Similar asymmetries have also been observed in water model experiments.^[41, 42] The asymmetries were more severe when the bottom wall of the water model was deeper.^[41] This suggests that intermittent inclusion asymmetries of the magnitude reported here may not be avoided by simply changing the nozzle design. Because the fluid velocities fluctuate greatly with time (Fig. 27, Part I), particles injected at other times would show a different distribution. Knowledge of such behavior is important, as particles which are transported deeper are more likely to become permanently entrapped in the steel.

B. Particle Trajectories

Figure 11 shows the computed trajectories of five typical particles for 220 seconds in the strand or until they contact a surface. The first trajectory (labeled 1) shows a particle which exited the left nozzle port, recirculated around the upper roll and eventually touched the top surface to be removed. The second trajectory shows a particle entering the mold from the center port, being drawn upward into the left side, recirculating and finally touching the top surface. Two trajectories (3 and 4) show particles flowing out the bottom of the domain, after wandering between the upper and lower rolls or moving directly with the flow down the narrow faces into the lower region. These particles would most likely be entrapped in the final product. The last trajectory (5) shows a particle that became entrapped at the wide face approximately 0.8m below the top surface. These irregular trajectories are similar to those observed in the water model (*Case I*). They confirm the effect of turbulent fluid structures on particle transport in actual steel casters.

C. Particle Removal and Capture Fractions

The removal and capture history in the strand of the four groups of particles of different sizes and densities are compared in Fig. 12 and Table IV. Particles exiting the nozzle ports could touch the outer nozzle walls, reach the top surface of the liquid pool to be removed, or become entrapped either by touching the solidification front (sides) or exiting the domain bottom. All four different types of particles in Fig. 12 have approximately the same capture and removal histories. Thus, the statistics in Table IV are independent of particle size and density. This is

expected because the small buoyancy force relative to drag for these small particles ($\leq 40\mu\text{m}$), as indicated in Eq. [2] produces small terminal velocities ($\leq 0.65\text{mm/s}$) relative to the fluid.

Approximately 8% of the particles that exit the nozzle ports are seen to be removed by the top surface. A further 8% of the particles touched the outside of the nozzle wall while recirculating in the liquid pool and might be removed, depending on the inclusion composition and nozzle properties. Most (90%) of these particles reached the surface within 47s (Fig. 12). Most (90%) of the captured particles flowed for less than 72s. The final statistics (Table IV) were compiled after all particles exiting the nozzle ports were either removed or captured, which took approximately 220 seconds. Approximately 51% of the particles were captured by the shell in the upper 2.4m of the strand where the shell thickness was less than 25mm (narrow face) or 26mm (wide face). Around 32% of the particles exited the domain from the bottom and would be captured at a deeper (and more interior) position in the solid slab. These results suggest that most (84%) of the small inclusions which enter the mold become entrapped in the final product. Thus, nozzle design and mold operation should focus on controlling flow at the meniscus to avoid the entrainment of new inclusions rather than altering the flow pattern to encourage removal of inclusions entering the mold. This conclusion may differ for large inclusions or if gas bubbles were present.

D. Inclusion Capture in Solid Steel Slabs after a Sudden Burst

A sudden “burst” of inclusions entering the liquid pool may occur in the continuous casting process during upstream events such as vortex entrainment of slag during a tundish level drop, release of a nozzle clog or other disturbance. ^[4, 43] Knowledge of the inclusion distribution in cast steel slabs caused by such a burst is important for the subsequent inspection and **dispositioning** of the product. The particle study in *Case 2-S* can be considered as a 9s burst of 40,000 inclusions entering the molten steel pool. By relating the total time traveled by each particle with the casting speed and its capture position, the distance of each of the 51% of the captured particles down the final solidified slab was calculated. The final positions of these particles are shown in Fig. 13, as transverse projections onto the wide and narrow faces. Zero on the vertical axis indicates the slice of the shell which was at the meniscus at the time when the first particle entered the strand (33.0s). All slices continuously moved downward with the whole shell at the casting speed during the process. The shadowed length in Fig. 13 is the distance traveled by the strand during the 9s burst. The simulation shows that the 220 seconds needed for all 51% particles to be captured corresponds to a length of around 7m. Most (78.5%) of those particles were captured within 1m above and below the zero-slice. Only a slight asymmetry of the capture positions can be observed from both view angles. This indicates that the flow asymmetries discussed earlier are not significant relative to particle capture. The significant asymmetries in defects sometimes observed in practice ^[44] must have been caused by much larger flow asymmetries resulting from transient events such as a slide gate opening change, or asymmetrical release of a nozzle clog or gas accumulation. Such events were not considered in this study, but are investigated elsewhere. ^[45]

E. Total Oxygen Distribution in Thin Steel Slabs

Total oxygen is often measured to evaluate the content of oxidized inclusions such as alumina in steel slabs. ^[1] It can also be calculated based on the computed positions and times of particle capture. The distribution of particles captured under a condition of continuous injection is found from the results in the previous section by assuming the 9s burst of particles to repeat every 9 seconds. The molten steel was assumed to exit the nozzle with a steady oxygen

content of 10ppm (by mass), from pure alumina (Al_2O_3) inclusions. The oxygen distribution in a typical cross section through the solidified slab was obtained by first projecting the entire computational domain ^[3] onto a transverse x-y section to define a 2-D grid of 3-D cells. The cell transverse dimensions, Δx and Δy , vary from 0.5mm to 6mm according to distance beneath the strand surface. The cell vertical dimension, Δz , is the length cast, 228.6mm, during the 9s burst. The total oxygen concentration in each cell, C_o , was calculated by dividing the mass of oxygen in all particles entrapped in that cell by the cell mass (including both cast steel and particles):

$$C_o = \frac{(48/102) M_p}{\rho(\Delta x \Delta y \Delta z) + (1 - \rho / \rho_p) M_p} \quad [8]$$

where $M_p = \sum_{i=1}^{N_c} \frac{\pi d_p^3 \rho_p}{6}$ and N_c are the total mass and number of particles entrapped in the cell.

The central region representing the area of the liquid pool at the domain exit was treated as a single large cell. This cell would contain all of the inclusions that exited the domain.

The number of particles entrapped in each cell, N_c , was obtained by summing the contributions from a series of 9s bursts. Each burst represents the contribution from a different time interval. The entrapment locations for each burst are obtained by translating the results in Fig. 13 vertically by $\Delta z * i$. The burst number i is an integer with a minimum value from the z coordinate of the last particle captured (-5.2m from Fig. 13) divided by Δz . The maximum i value is the domain bottom coordinate (+1.9m) divided by Δz . The final particle distribution is obtained from the sum of the entrapment distributions from each value of i within this range.

The results are given in the cross section of the steel strand shown in Fig. 14. The dashed line represents the boundaries of the central large cell and is the solidification front at the domain exit (2.4m below meniscus). The highest total oxygen content (about 170ppm) is predicted near the corners, closely followed by intermittent patches on the narrow faces. Intermittent patches with high oxygen concentrations (50-150ppm) are also found in the middle region of the strand (approximately 10-20mm beneath the slab surface). These results indicate that most of the captured particles (69%) are entrapped within the shell approximately 0.4-1.5m below meniscus (corresponding to a shell thickness of 10-20mm). The finding of increased inclusion capture across the slab width towards the narrow faces agrees with previous measurements ^[17] and calculations. ^[13] Other measurements find sliver defects concentrated at the surface more towards the wide face centerlines. This is only a slight trend here, owing to impingement from the bottom central port. More severe centerline concentrations would have been predicted if some of the inclusions hitting the top surface were able to continue moving with the flow towards the SEN before being captured in the steel shell at the meniscus. Alternatively, the larger particles which contribute the most to sliver defects have more complex entrapment criteria, such as being pushed along at the solidification front before capture.

Figure 15 reveals the oxygen content along the two centerlines shown in Fig. 14. Higher inclusion concentrations are found towards the surfaces. Similar variations in total oxygen distribution have been measured in other steel slabs, in which particles were found to concentrate most within 20mm of the slab surface. ^[46] Small regions with high oxygen content are also distributed sparsely towards the center of the wide faces. This is caused by groups of particles from the center nozzle port. Small patches with low total oxygen close to zero are randomly

distributed in the cross section, indicating the effects of turbulent motion of the fluid. Asymmetries can be observed in this symmetrical domain, confirming the influence of fluid instabilities on particle transport and capture. No significant difference is observed between the inside and outside radius, which is consistent with the lack of buoyancy of the small particles considered in this work. In practice, large inclusions are generally of more relevance to quality problems, so future work will focus on developing a capture model for large particles.

V. CONCLUSIONS

Lagrangian computations of particle transport during continuous casting of steel slabs were performed in this study. Time-dependent fluid velocity fields obtained from LES presented in Part I were employed in the particle computations. The computational model was first validated with measurements in a full-scale water model. It was then applied to simulate the transport and capture of 10 μ m and 40 μ m inclusions in a thin slab steel caster. Following conclusions are reached, based on the results of this study:

- (1) Complex particle trajectories are seen in both the water model and the actual steel caster, showing the important influence of turbulence on particle transport. The simulated particle trajectories as well as the predicted removal fractions are in agreement with water model measurements.
- (2) Particle removal was independent of initial position at the nozzle port, for the relatively uniform fluid velocity profile at the nozzle exit ports in the water model study.
- (3) A comparison of particle removal fractions obtained from 2,500 and 500 particle groups suggests that increasing the number of particles improves the accuracy of removal predictions for later times (e.g. 10-100s). At least 2500 particles are required to obtain accuracy within $\pm 3\%$. Particle removal at early times (e.g. ≤ 10 s) is governed by chaotic fluctuations of the flow, which generate variations of $\pm 5\%$.
- (4) Asymmetric particle distributions are observed in the liquid pool, which are caused by transients of fluid turbulence, rather than imposed by the inlet condition at nozzle ports. This only leads to slight asymmetries in the particle distribution in the final product.
- (5) The top surface is predicted to remove only 8% of small particles (10 μ m and 40 μ m) in the thin slab steel caster. An equal fraction touches the outside of the nozzle walls in the mold. These removal fractions are independent of both particle size and density, owing to the inability of the small, low-buoyancy particles simulated here to deviate significantly from the surrounding fluid flow.
- (6) The computation shows that after a 9s sudden burst of particles enters the steel caster, about 4 minutes are needed for all of them to be captured or removed for the casting conditions assumed here. The captured particles concentrate mainly within a 2-m long section of slab.
- (7) With a steady oxygen content of 10ppm from inclusions in the molten steel supplied from the nozzle ports, intermittent patches of high oxygen content (50-150ppm) are found concentrated within 10-20mm beneath the slab surface, especially near the corner, and towards the narrow faces.

The present study confirms the importance of flow transients in affecting the transport and capture of inclusions during continuous casting.

ACKNOWLEDGEMENTS

The authors thank the National Science Foundation (Grant DMI-01-15486) which made this research possible. The work is also supported by the member companies of the Continuous Casting Consortium at University of Illinois at Urbana-Champaign (UIUC). Special thanks are due to Ron O'Malley, for plant data and insights into inclusion behavior, and to the National Center for Supercomputing Applications (NCSA) at UIUC for computational facilities.

NOMENCLATURE

\mathbf{v}	velocity vector	\mathbf{g}	gravity acceleration vector
\mathbf{x}	displacement vector	\mathbf{F}_{saff}	Saffman lift force defined by Eq. [4]
t	time	$\boldsymbol{\omega}$	vorticity of fluid
ρ	density	t_v	particle response time defined by Eq. [7]
ν_0	kinematic viscosity of fluid	σ_u	standard deviation of u
μ_0	dynamic viscosity of fluid	Subscripts:	
d	diameter	p	particle
m	mass	none	steel
M	total mass	C	cell (Eq. [8])
N	number (integer)	i	particle burst number

REFERENCES

1. L. Zhang and B.G. Thomas: "State of the Art in Evaluation and Control of Steel Cleanliness", *ISIJ International*, 2003, vol. 43 (3), pp. 271-91.
2. W.H. Emling, T.A. Waugaman, S.L. Feldbauer and A.W. Cramb: "Subsurface Mold Slag Entrainment in Ultra-Low Carbon Steels", in *Steelmaking Conference Proceedings*, vol. 77, (Chicago, IL, April 13-16, 1997), ISS, Warrendale, PA, 1994, pp. 371-79.
3. Q. Yuan, B.G. Thomas and S.P. Vanka: "Study of Transient Flow and Particle Transport during Continuous Casting of Steel Slabs: Part I. Fluid Flow", *Metallurgical and Materials Transactions B*, 2003, accepted.
4. B.G. Thomas: "Chapter 14: Fluid Flow in the Mold", in *The Making, Shaping and Treating of Steel, 11th Edition, Casting Volume*, A.W. Cramb, ed., The AISE Steel Foundation, 2003, p. 24.
5. J. Herbertson, Q.L. He, P.J. Flint and R.B. Mahapatra: "Modeling of Metal Delivery to Continuous Casting Moulds", in *Steelmaking Conf. Proceedings*, vol. 74, ISS, Warrendale, PA, 1991, pp. 171-85.
6. E. Loth: "Numerical Approaches for Motion of Dispersed Particles, Droplets and Bubbles", *Progress in Energy and Combustion Science*, 2000, vol. 26, pp. 161-223.
7. K.D. Squire and J.K. Eaton: "Particle Response and Turbulence Modification in Isotropic Turbulence", *Physics of Fluids*, 1990, vol. 2 (7), pp. 1191-203.
8. S. Elghobashi and G.C. Truesdell: "Direct Numerical Simulation of Particle Dispersion in a Decaying Isotropic Turbulence", *Journal of Fluid Mechanics*, 1992, vol. 242, pp. 655-700.

9. Q. Wang and K.D. Squire: "Large Eddy Simulation of Particle Deposition in a Vertical Turbulent Channel Flow", *Int. J. Multiphase Flow*, 1996, vol. 22 (4), pp. 667-83.
10. Q. Wang and K.D. Squire: "Large Eddy Simulation of Particle-Laden Channel Flow", *Physics of Fluids*, 1996, vol. 8 (5), pp. 1207-23.
11. M.S. Boivin and K.D. Squire: "On the Prediction of Gas-Solid Flows with Two-Way Coupling Using Large-Eddy Simulation", *Physics of Fluids*, 2000, vol. 12 (8), pp. 2080-90.
12. H. Zhang and G. Ahmadi: "Aerosol Particle Transport and Deposition in Vertical and Horizontal Turbulent Duct Flow", *Journal of Fluid Mechanics*, 2000, vol. 406 (55-80).
13. B. Grimm, P. Andrzejewski, K. Muller and K.-H. Tacke: "Inclusions in Continuously Cast Steel Slabs-Numerical Model and Validation", *Steel Res.*, 1999, vol. 70 (10).
14. B.G. Thomas and L. Zhang: "Mathematical Modeling of Fluid Flow in Continuous Casting", *ISIJ International*, 2001, vol. 41 (10), pp. 1181-93.
15. S. Asai and J. Szekely: "Turbulent Flow and its Effects in Continuous Casting", *Ironmaking Steelmaking*, 1975, vol. 3, p. 205.
16. B.G. Thomas, A. Dennisov and H. Bai: "Behavior of Argon Bubbles during Continuous Casting of Steel", in *Steelmaking Conference Proceedings*, vol. 80, (Chicago, IL, April 13-16, 1997), ISS, Warrendale, PA., 1997, pp. 375-84.
17. R.C. Sussman, M. Burns, X. Huang and B.G. Thomas: "Inclusion Particle Behavior in a Continuous Slab Casting Mold", in *10th Process Technology Conference Proc.*, vol. 10, Iron and Steel Society, Warrendale, PA, 1992, pp. 291-304.
18. Y. Ho, C. Chen and W. Hwang: "Analysis of Molten Steel Flow in Slab Continuous Caster Mold", *ISIJ International*, 1994, vol. 34 (3), pp. 255-64.
19. Y. Ho and W. Hwang: "The Analysis of Molten Steel Flow in Billet Continuous Casting", *ISIJ International*, 1996, vol. 36 (8), pp. 1030-35.
20. C.M. Winkler, S.L. Rani and S.P. Vanka: "Large Eddy Simulations of Particle Deposition in a Fully Developed Turbulent Square Duct Flow", *Physics of Fluids*, in review, 2003.
21. C.M. Winkler, S.L. Rani and S.P. Vanka: "Preferential Concentration of Particles in a Fully Developed Turbulent Square Duct Flow", *Int. J. Multiphase Flow*, in review, 2003.
22. S.L. Rani: *Direct Numerical Simulations of Two-Way Coupling Effects in a Particle-Laden Turbulent Pipe Flow & Evaluation of the Equilibrium Eulerian Approach for the Evolution of Particle Concentration in Isotropic Turbulence*, Ph.D. Thesis, University of Illinois at Urbana-Champaign, 2002.
23. C. Crowe, M. Sommerfeld and Y. Tsinji: *Multiphase Flows with Droplets and Particles*, CRC Press, pp. 23-95.
24. D.R. Uhlmann and B. Chalmers: "Interaction Between Particles and a Solid-Liquid Interface", *Journal of Applied Physics*, 1964, vol. 35 (10), pp. 2986-93.
25. J. Potschke and V. Rogge: "On The Behavior of Foreign Particle at An Advancing Solid-Liquid Interface", *J. Crystal Growth*, 1989, vol. 94, pp. 726-38.

26. D. Shangguan, S. Ahuja and D.M. Stefanescu: "An Analytical Model for the Interaction between an Insoluble Particle and an Advancing Solid/Liquid Interface", *Met. Trans. A*, 1992, vol. 23A (2), pp. 669-80.
27. Q. Han and J.D. Hunt: "Particle Pushing: the Attachment of Particles on the Solid-Liquid Interface during Fluid Flow", *J. Crystal Growth*, 1994, vol. 140, pp. 406-13.
28. Q. Han and J.D. Hunt: "Particle Pushing: Critical Flow Rate Required to Put Particles into Motion", *J. Crystal Growth*, 1995, vol. 152, pp. 221-27.
29. D.M. Stefanescu and A.V. Catalina: "Note: Calculation of The Critical Velocity for The Pushing/Engulfment Transition of Nonmetallic Inclusions in Steel", *ISIJ Int.*, 1998, vol. 38 (5), pp. 503-05.
30. Y. Wang, M. Valdez and S. Sridhar: "Liquid and Solid Inclusions at Advancing Steel Solidification Fronts", *Z. Metallkd.*, 2002, vol. 93 (1), pp. 12-20.
31. G. Wilde and J.H. Perepezko: "Experimental Study of Particle Incorporation during Dendritic Solidification", *Materials Science & Engineering A*, 2000, vol. 283, pp. 25-37.
32. Q. Yuan: University of Illinois, private communication, 2003.
33. B.G. Thomas, R.J. O'Malley and D.T. Stone: "Measurement of temperature, solidification, and microstructure in a continuous cast thin slab", *Modeling of Casting, Welding, and Advanced Solidification Processes*, B.G. Thomas and C. Beckermann, eds., (San Diego, CA), TMS, Warrendale, PA, 1998, vol. VIII, pp. 1185-99.
34. W.H. Press, B.P. Flannery, S.A. Teukolsky and W.T. Vetterling: *Numerical Recipes*, Cambridge University Press, New York, NY, 1988, p. 963.
35. Y. Miki and B.G. Thomas: "Modeling of Inclusion Removal in a Tundish", *Metallurgical and Materials Transactions B*, 1999, vol. 30B (4), pp. 639-54.
36. B.G. Thomas, X. Huang and R.C. Sussman: "Simulation of Argon Gas Flow Effects in a Continuous Slab Caster", *Metall. Trans. B*, 1994, vol. 25B (4), pp. 527-47.
37. B.G. Thomas, Q. Yuan, S. Sivaramakrishnan and S.P. Vanka: "Transient Fluid Flow in the Continuous Steel-Slab Casting Mold", *JOM-e (Journal of Metals Electronic Edition)*, <http://www.tms.org/pubs/journals/JOM/0201/Thomas/Thomas-0201.html>, 2002.
38. B.G. Thomas, R. O'Malley, T. Shi, Y. Meng, D. Creech and D. Stone: "Validation of Fluid Flow and Solidification Simulation of a Continuous Thin Slab Caster", in *Modeling of Casting, Welding, and Advanced Solidification Processes*, vol. IX, Shaker Verlag GmbH, Aachen, Germany, 2000, pp. 769-76.
39. R.J. O'Malley: "Observations of Various Steady State and Dynamic Thermal Behaviors in a Continuous Casting Mold", *82nd Steelmaking Conference*, TMS, ed., (Chicago, IL), TMS, 1999, p. 21.
40. R.J. O'Malley: Mansfield, OH, private communication, 2003.
41. D. Gupta and A.K. Lahiri: "A Water Model Study of the Flow Asymmetry Inside a Continuous Slab Casting Mold", *Metallurgical and Materials Transactions B*, 1996, vol. 27B (5), pp. 757-64.

42. D. Gupta, S. Chakraborty and A.K. Lahiri: "Asymmetry and Oscillation of the Fluid Flow Pattern in a Continuous Casting Mould: a Water Model Study", *ISIJ Int.*, 1997, vol. 37 (7), pp. 654-58.
43. J.H. Schade, R.J. O'Malley, F.L. Kemeny, Y. Sahai and D.J. Zacharias: "Chapter 13: Tundish Operations", in *The Making, Shaping and Treating of Steel, 11th Edition, Casting Volume*, A.W. Cramb, ed., The AISE Steel Foundation, 2003, p. 70.
44. J. Knoepke, M. Hubbard, J. Kelly, R. Kittridge and J. Lucas: "Pencil Blister Reduction at Inland Steel Company", in *Steelmaking Conference Proceedings*, vol. 77, (Chicago, IL, March 20-23, 1994), ISS, Warrendale, PA, 1994, pp. 381-88.
45. X. Huang and B.G. Thomas: "Modeling of Transient Flow Phenomena in Continuous Casting of Steel", *Canadian Metall. Quart.*, 1998, vol. 37 (304), pp. 197-212.
46. L. Zhang and B.G. Thomas: "Inclusion Investigation during Clean Steel Production at Baosteel", *ISSTech 2003*, (Indianapolis, IN), 2003, pp. 577-92.

LIST OF FIGURES AND TABLES

- Figure 1. Schematics of the process of continuous casting of steel.**
- Figure 2. Schematics of the computational domain of (a) the full-scale standard thickness slab water model (*Case 1*) and (b) the thin slab steel caster (*Case 2-S*).**
- Figure 3. Variation of primary dendrite arm spacing (PDAS) along distance below meniscus. ^[33]**
- Figure 4. Distribution of the 15,000 particles in *Case 1* at four time instants after their injection, view from wide face (left) and narrow face (right).**
- Figure 5. Representative particle trajectories observed in the computation of *Case 1*.**
- Figure 6. Initial positions at the nozzle port of (a) all 15,000 particles and those removed to the top surface in (b) 0-10 s and (c) 0-100 s after entering the liquid-pool (*Case 1*).**
- Figure 7. Particle removal to the top surface in *Case 1*.**
- Figure 8. Inclusion entrapment positions in nozzle inner wall (*Case 2-S*).**
- Figure 9. Locations where inclusions exit nozzle ports (*Case 2-S*).**
- Figure 10. Distribution of moving particles at three instants (*Case 2-S*).**
- Figure 11. Predicted representative particle trajectories in an actual steel caster (*Case 2-S*).**
- Figure 12. Particle removal and entrapment in the steel caster (*Case 2-S*).**
- Figure 13. Particle entrapment location for 9s injection: view from wide face (left) and from narrow face (right).**
- Figure 14. Predicted oxygen concentration averaged in the length direction (10ppm oxygen at nozzle ports).**

Figure 15. Oxygen content along the centerlines in Fig. 14.

Table I. Properties and conditions of the particle simulations.

Table II. Details of particle injection during simulation (*Case 1*).

Table III. Comparison of fractions of particles removed by the screen in *Case 1*.

Table IV. Statistics of particle entrapment and removal in *Case 2-S*.

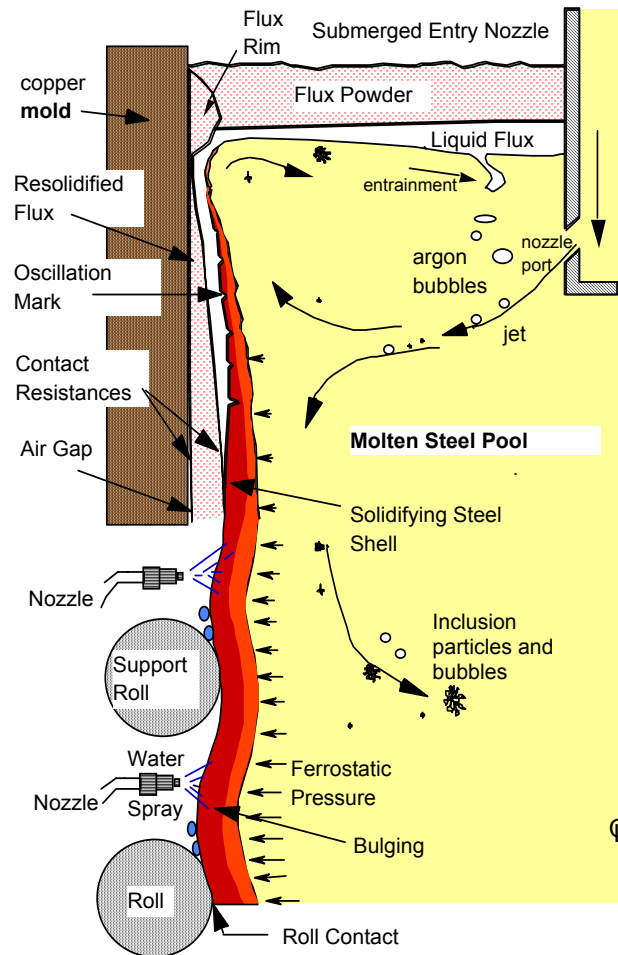


Figure 1. Schematics of the process of continuous casting of steel.

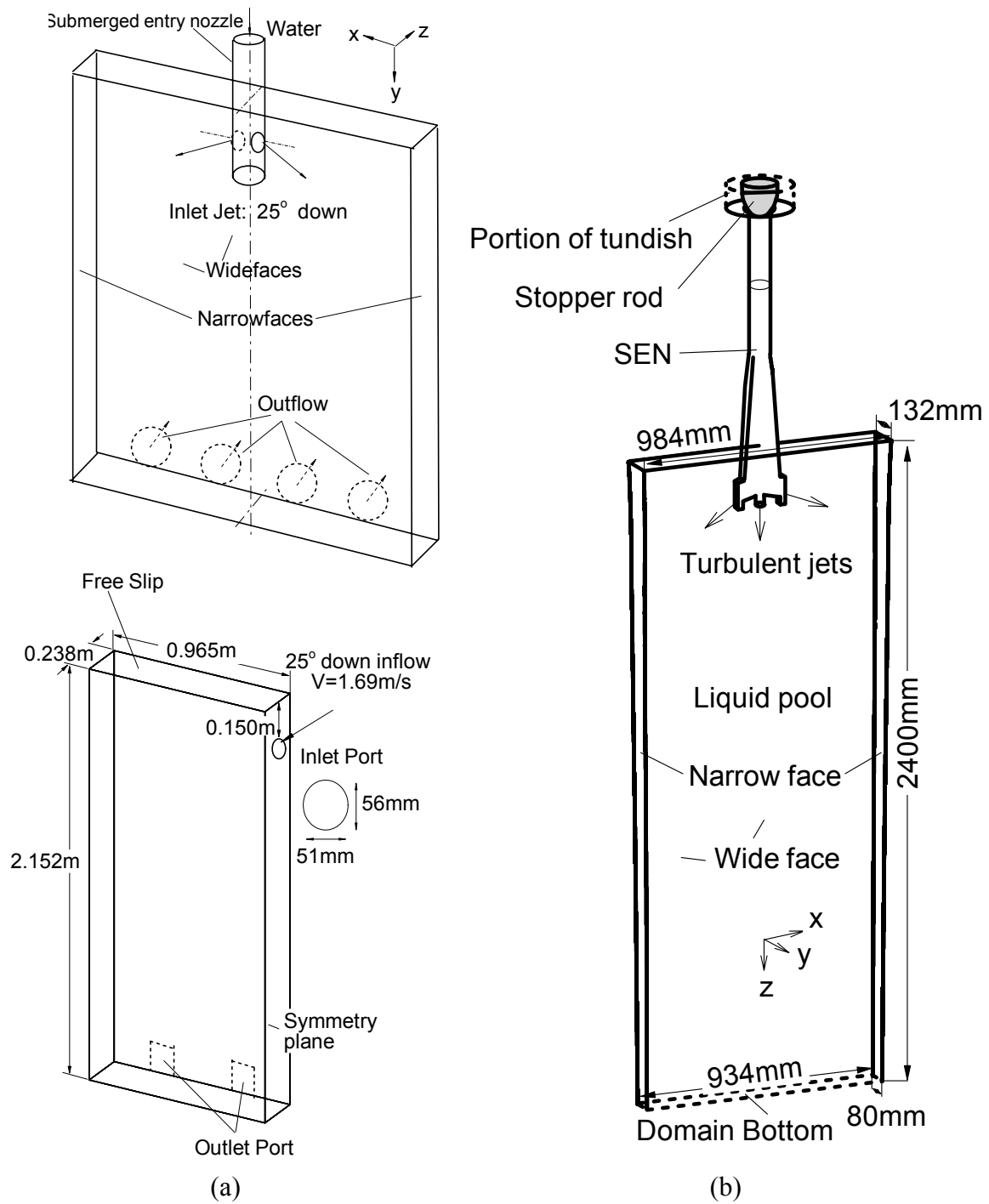


Figure 2. Schematics of the computational domain of (a) the full-scale standard thickness slab water model (*Case 1*) and (b) the thin slab steel caster (*Case 2-S*).

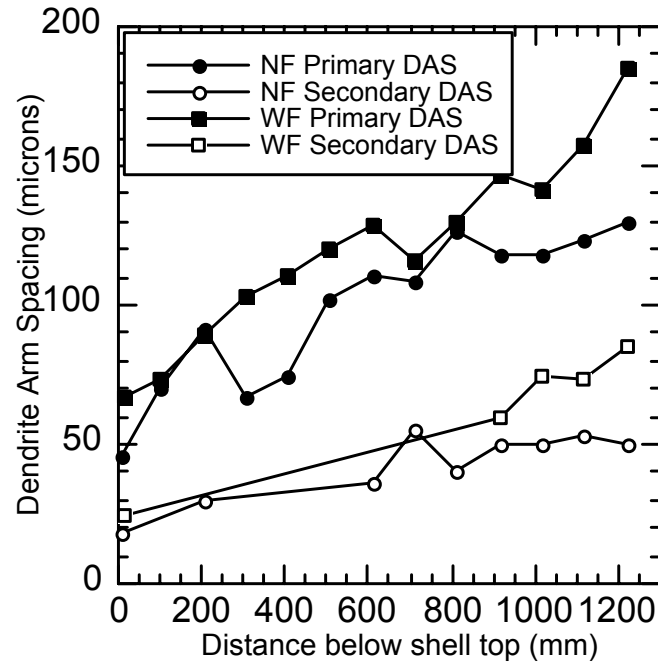


Figure 3. Variation of primary dendrite arm spacing (PDAS)
along distance below meniscus. ^[33]

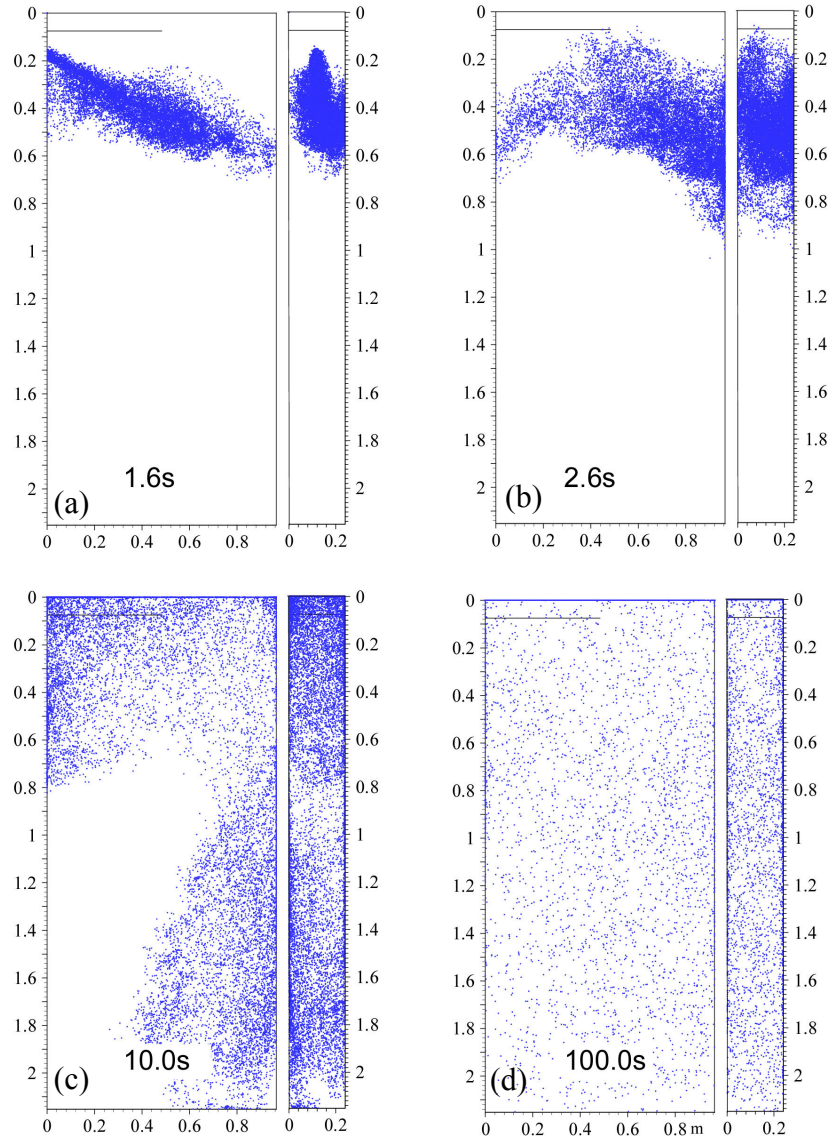


Figure 4. Distribution of the 15,000 particles in *Case 1* at four time instants after their injection, view from wide face (left) and narrow face (right).

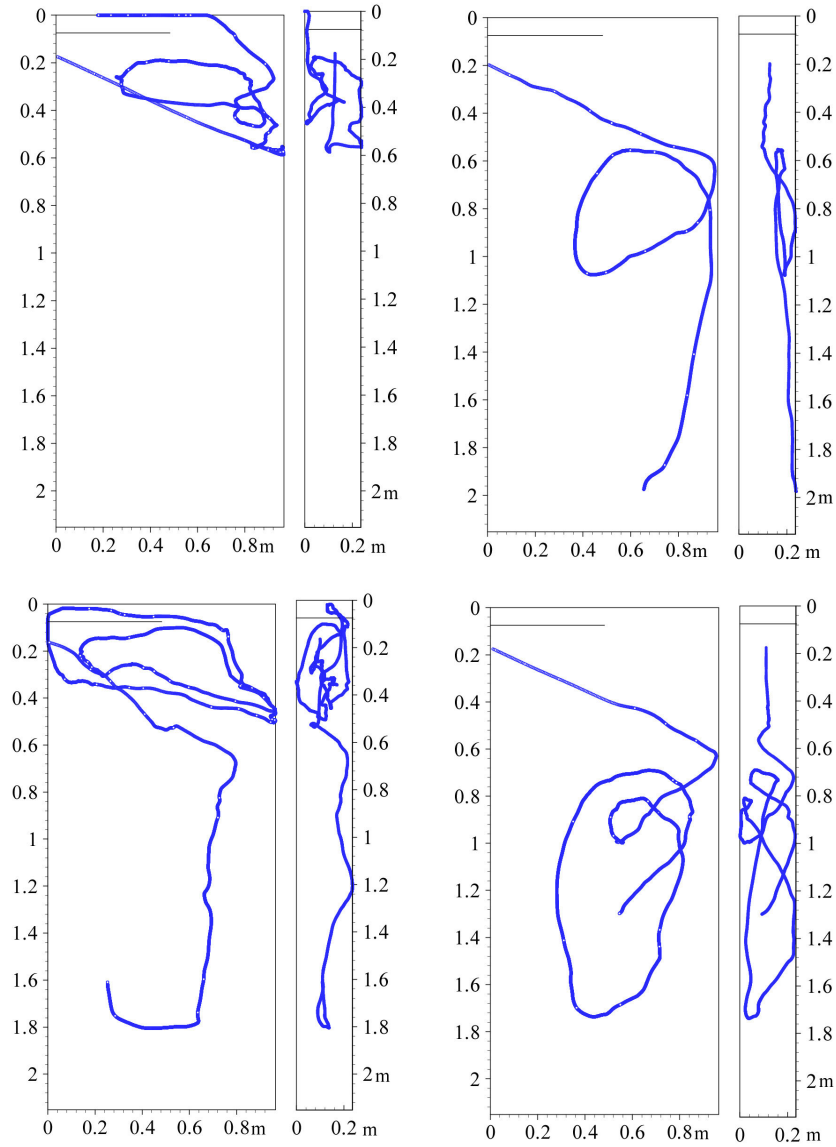


Figure 5. Representative particle trajectories observed in the computation of *Case 1*.

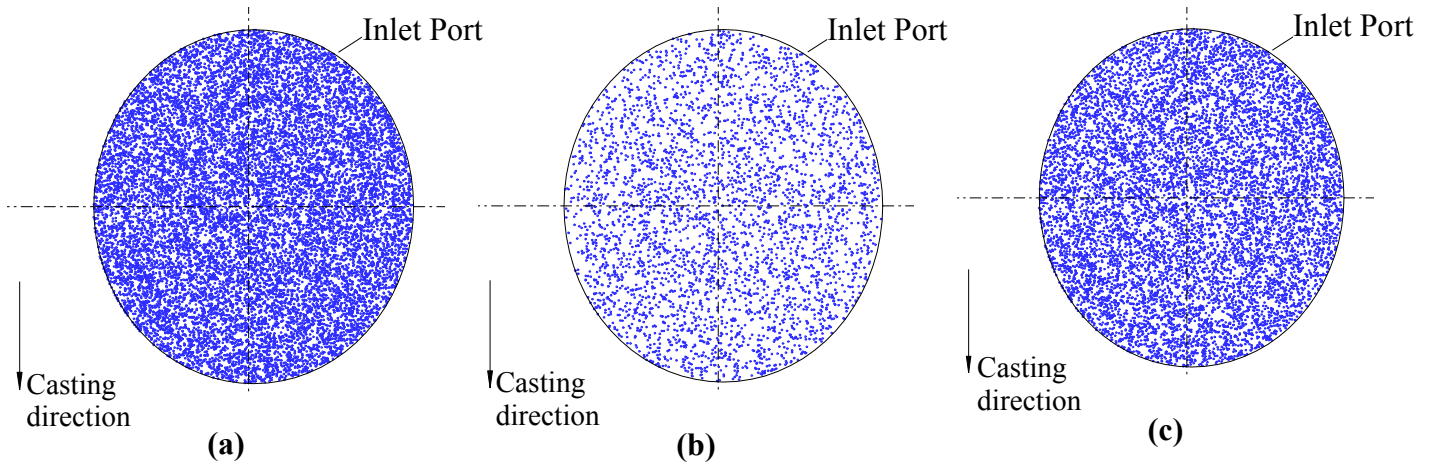


Figure 6. Initial positions at the nozzle port of (a) all 15,000 particles and those removed to the top surface in (b) 0-10 s and (c) 0-100 s after entering the liquid-pool (*Case 1*).

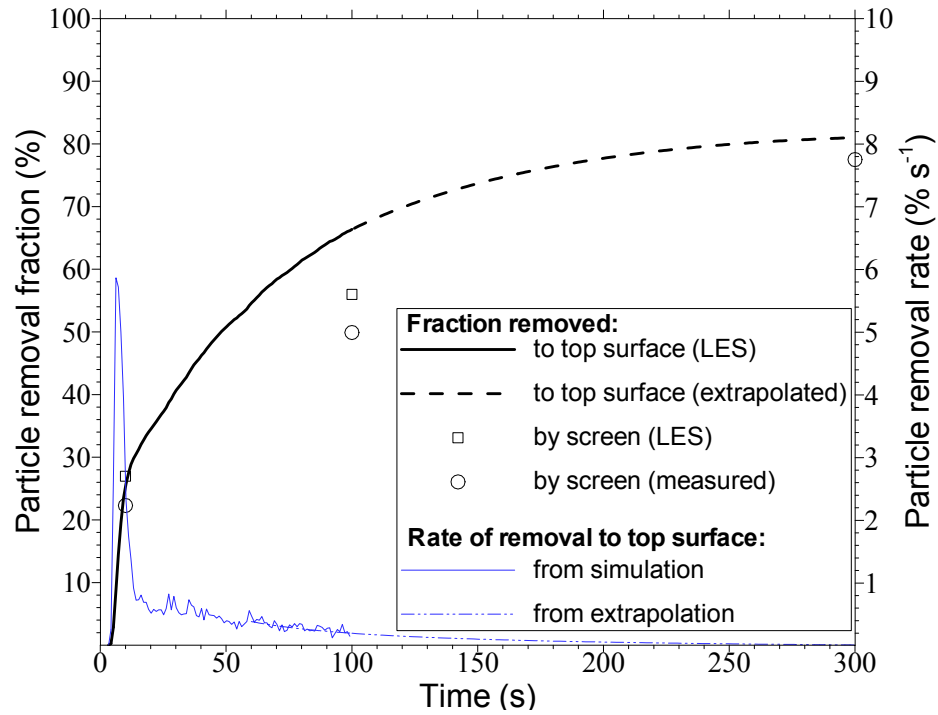


Figure 7. Particle removal to the top surface in *Case 1*.

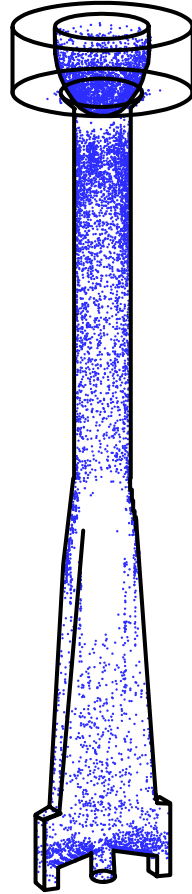


Figure 8. Inclusion entrapment positions in nozzle inner wall (*Case 2-S*).

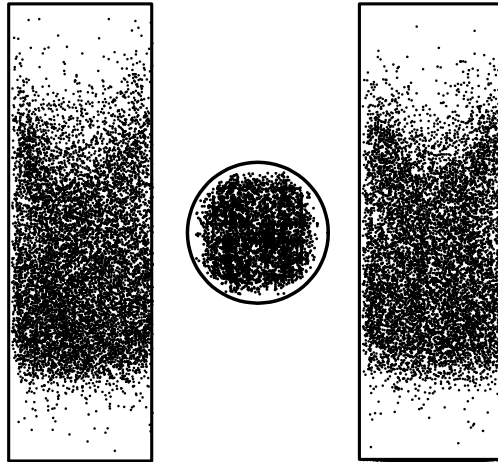


Figure 9. Locations where inclusions exit nozzle ports (*Case 2-S*).

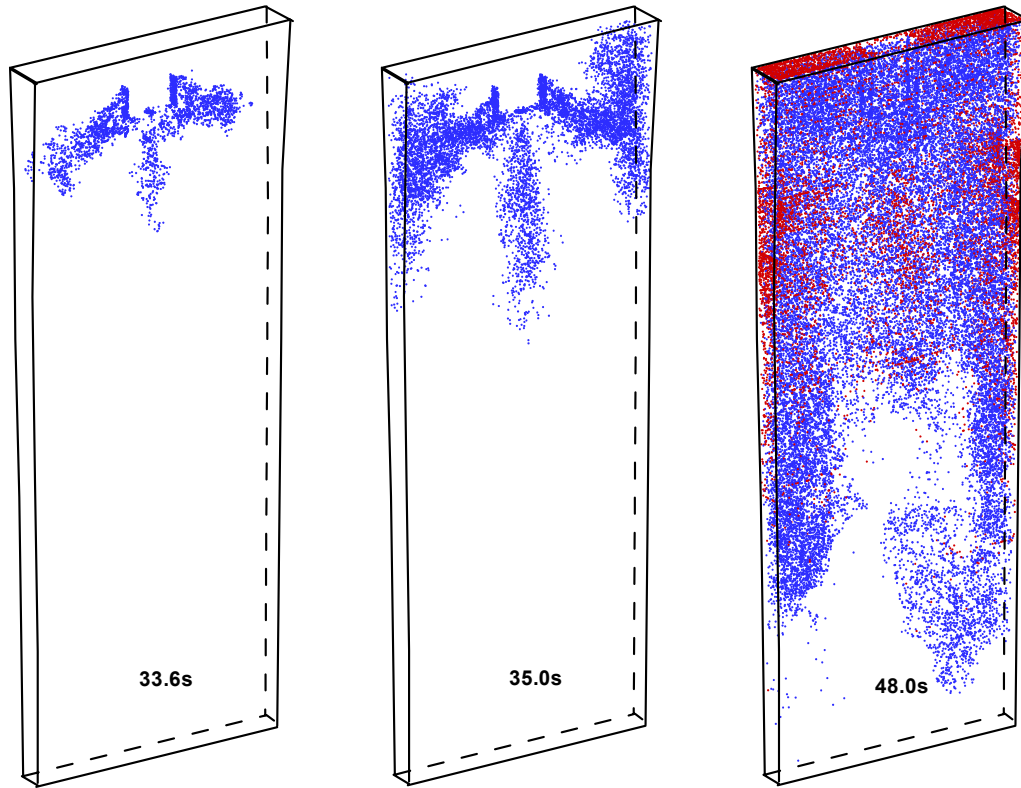


Figure 10. Distribution of moving particles at three instants (*Case 2-S*).

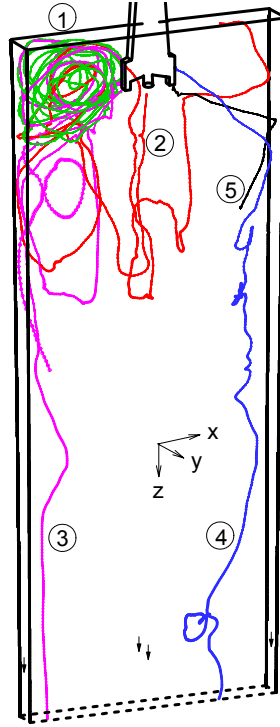


Figure 11. Predicted representative particle trajectories in the steel caster (*Case 2-S*).

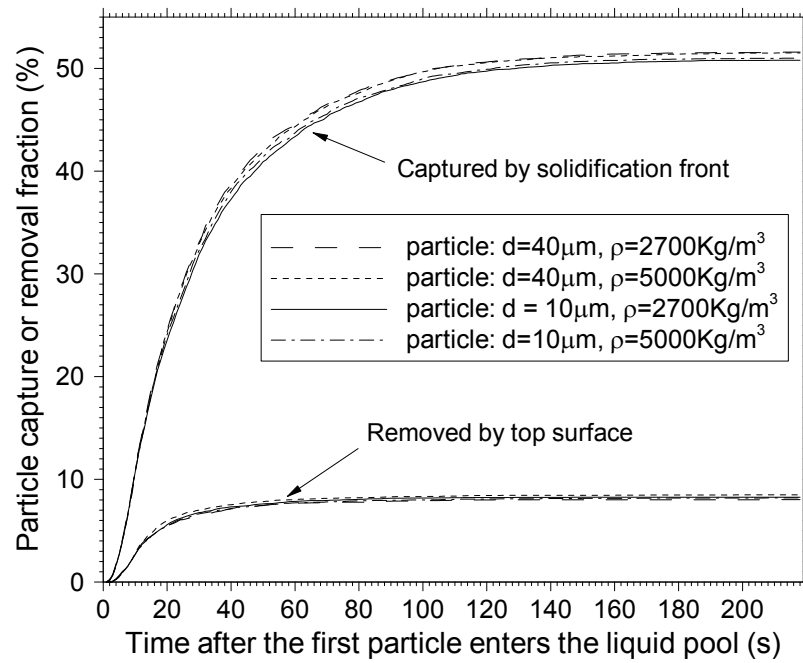


Figure 12. Particle removal and entrapment in the steel caster (*Case 2-S*).

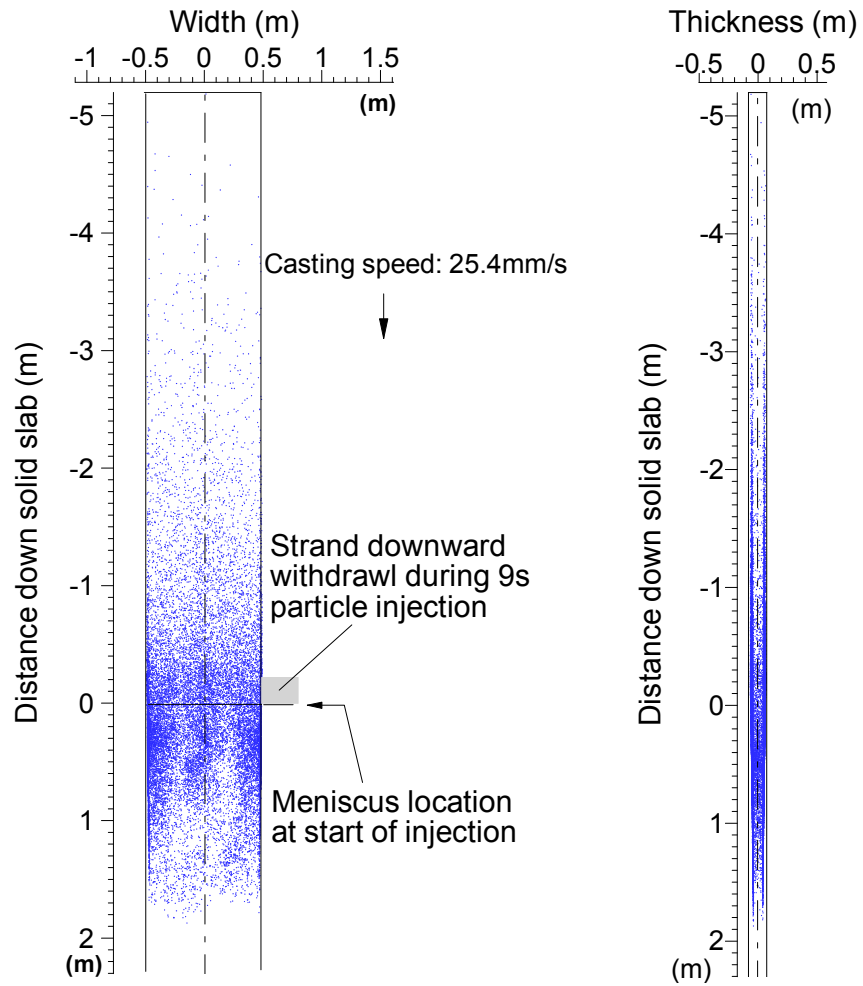
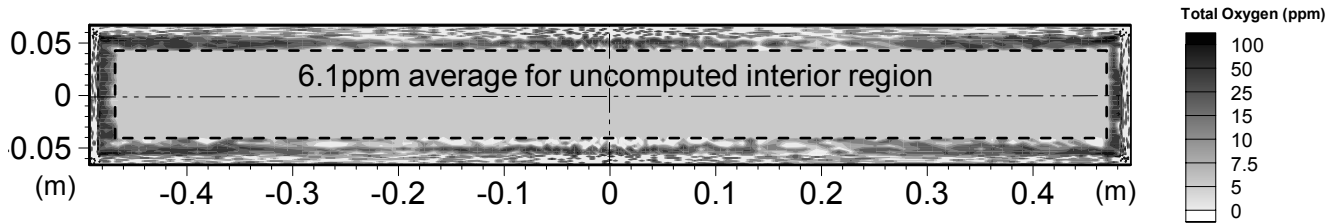


Figure 13. Particle entrapment location for 9s injection: view from wide face (left) and from narrow face (right).



**Figure 14. Predicted oxygen concentration averaged in the length direction
(10ppm oxygen at nozzle ports).**

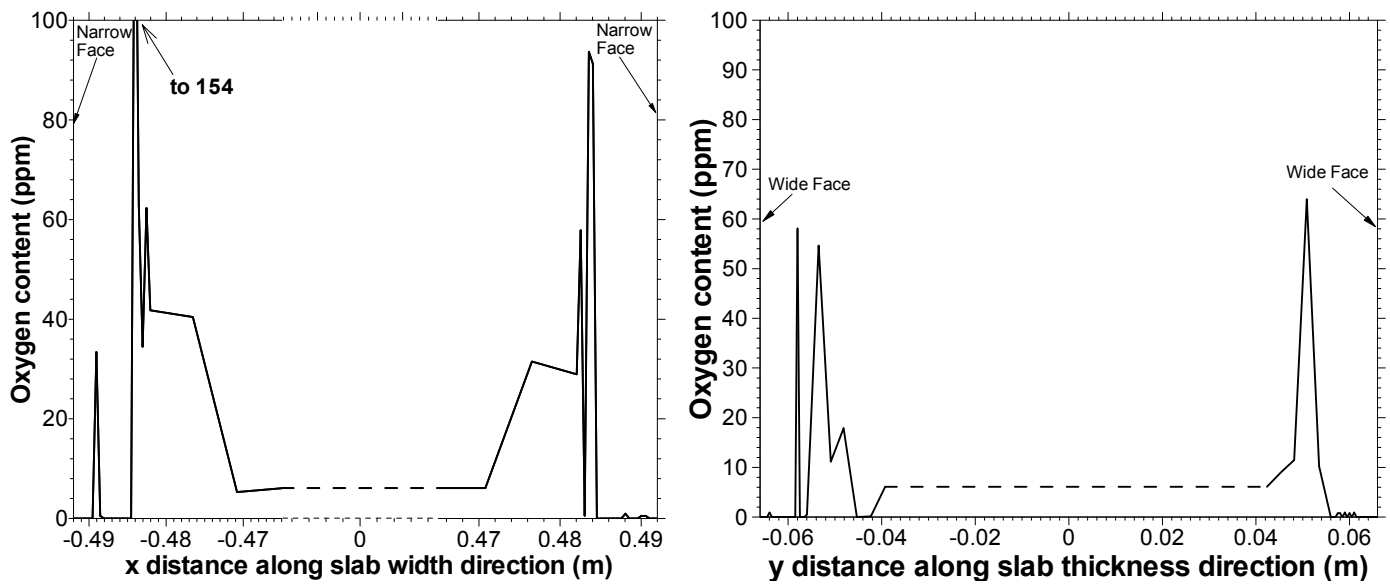


Figure 15. Oxygen content along the centerlines in Fig. 14.

Table I. Properties and conditions of particle simulations.

Parameter/Property	<i>Case 1</i>	<i>Case 2-S</i>
Mold Width (mm)	1830	984
Mold Thickness (mm)	238	132
Water Model Length (mm)	2152	-
Mold Length (mm)	-	1200
Domain Width (mm)		
- top	915	984
- bottom	915	934.04
Domain Thickness (mm)		
- top	238	132
- bottom	238	79.48
Domain Length (mm)	2152	2400
Nozzle Port Height \times Thickness (mm \times mm)	51 \times 56 (see Fig.2)	75 \times 32 (inner bore)
Bottom nozzle Port Diameter (mm)	-	32
SEN Submergence Depth (mm)	150	127
Casting Speed (mm/s)	15.2	25.4
Fluid Dynamic Viscosity (m ² /s)	1.0×10^{-6}	7.98×10^{-7}
Fluid Density (kg/m ³)	1000	7020
Particle Density (kg/m ³)	988	2700 and 5000
Particle Diameter (μ m)	3800	10 and 40
Argon Gas Injection (l/m ³)	0%	0%

Table II. Details of particle injection during simulation (*Case 1*).

Number of particles	Time of introduction
15000	0s – 1.6s
500	2s – 2.4s
500	4s – 4.4s
500	6s – 6.4s
500	8s – 8.4s
500	10s – 10.4s

Table III. Comparison of fractions of particles removed by the screen in *Case 1*.

		0-10 seconds	10-100 seconds
LES	500 particle groups		
	<i>1</i>	27.2%	23.4%
	<i>2</i>	17.8%	27.2%
	<i>3</i>	26.2%	23.0%
	<i>4</i>	23.8%	23.2%
	<i>5</i>	33.0%	18.2%
	<i>Average</i>	25.6%	23.0%
	<i>Standard Deviation</i>	5.5%	2.9%
	2500 particle groups		
	<i>1</i>	27.2%	25.9%
	<i>2</i>	26.8%	27.1%
	<i>3</i>	20.0%	26.5%
	<i>4</i>	23.3%	27.8%
	<i>5</i>	31.8%	24.1%
	<i>6</i>	32.6%	24.9%
	<i>Average</i>	27.0%	26.1%
	<i>Standard Deviation</i>	4.8%	1.4%
Experiment		22.3%	27.6%

Table IV. Statistics of particle entrapment and removal in *Case 2-S*.

		Group 1	Group 2	Group 3	Group 4	Average
Diameter (μm)		40	40	10	10	-
Density (kg/m^3)		5000	2700	5000	2700	-
Fraction of	Captured by shell	51.58%	51.51%	50.79%	51.00%	51.22%
	Captured deeper	32.22%	32.07%	32.77%	32.54%	32.40%
	Removed by top surface	8.03%	8.49%	8.23%	8.20%	8.24%
	Removed by nozzle wall	8.12%	7.83%	8.03%	8.15%	8.03%